RSC Advances

PAPER

View Article Online
View Journal | View Issue

Cite this: *RSC Adv.*, 2026, **16**, 3602

A high-copper-content metal–organic framework with potential antibacterial activities

Boya Liu * and Xueqi Zheng

Received 26th October 2025
Accepted 4th January 2026

DOI: 10.1039/d5ra08205f

rsc.li/rsc-advances

Despite recent significant advancements in antibacterial applications of copper-based metal–organic frameworks (Cu MOFs), the synthesis of a high-copper-content MOF remains elusive. Here we proposed a multi-coordination strategy through a direct solvothermal reaction of Cu ions and formic acid, which yielded a three-dimensional MOF (denoted as **Cu-FA**) containing 32% Cu. Through single crystal X-ray diffraction analyses, the precise spatial structure of **Cu-FA** was determined. Two types of Cu···O coordination bonds with varying bond energies were found in **Cu-FA**, enabling a multistage Cu release protocol to balance the antibacterial efficacy and biocompatibility. As a result, **Cu-FA** presented significant antibacterial activity against *Escherichia coli*, with an inactivation rate of 99.76%. Overall, this study not only establishes a viable strategy for synthesizing high-copper-content MOFs, deepening the understanding of their multilayer structures, but also providing a new insight into the exploration of antibacterial applications.

1. Introduction

Copper metal–organic frameworks (Cu MOFs), formed by the coordination of Cu ions and organic ligands, have attracted great attention in antibacterial applications due to their controllable Cu ion releases, programmable structures, high specific surface areas, *etc.*[1–5] Under the acidic microenvironment of bacteria-infected wounds,[6–9] free Cu ions can be released from Cu MOFs, exhibiting toxic effects on bacteria, including the promotion of reactive oxygen species (ROS) and induced oxidative damage.[10,11] To improve the antibacterial activity of Cu MOFs, strategies including heterometallic doping,[12–14] surface modification and loading,[15–17] have been developed. However, the mass effect of organic ligands has rarely been taken into consideration. Excessively bulky organic ligands tend to cause a decrease in Cu^{2+} loading rate, thereby compromising their antibacterial activity. Furthermore, for a high-Cu-content MOF, an intrinsic multistage copper release mechanism is indispensable to avoid the potential cytotoxicity caused by excessive copper concentration.

Carboxylic groups with two coordinative oxygen sites exhibit strong binding capacity to various metals, such as Cu, Ni, Fe, Co, *etc.*[18–23] Notably, the carbonyl oxygen and hydroxyl oxygen in carboxylic groups exhibit distinct coordination capacities to metals, leading to different bond energies and acid-responsive behaviours. Consequently, carboxylate-based Cu MOFs provide a chance to achieve multistage Cu release protocol. Specially, due to the weaker coordination ability of hydroxyl oxygen than carbonyl oxygen, C–O···Cu coordination bonds will be preferentially cleaved, followed by C–O···Cu bonds. Consequently, formic acid, the simplest carboxylate-based linker, is the best candidate to construct high-Cu-content MOFs. Though formate-based MOFs has been reported,[24–27] such formate-based Cu-MOFs with high Cu^{2+} loading and multiple Cu release protocols has not been systematically investigated for antibacterial applications.

Herein, we reported a high-Cu-content MOF constructed by the coordinating of Cu^{2+} and formic acid, named **Cu-FA** (Fig. 1a and b). Due to the high-quality single crystals of **Cu-FA**, the precise spatial structure of **Cu-FA** was determined by single crystal X-ray diffraction (SCXRD) analyses. The results revealed a high Cu content of 32% for the three-dimensional framework, and two types of Cu···O coordination bonds featured by bond lengths of 1.97 and 2.50 and Å. Furthermore, the bond energies in the two Cu···O coordination bonds lead to different acid stability and multistage release of Cu^{2+}. As confirmed by inductively coupled plasma optical emission spectroscopy (ICP-OES), sustained Cu^{2+} release was maintained over 72 h, avoiding the rapid surge of Cu^{2+} concentration. Subsequently, *in vitro* experiments demonstrated that **Cu-FA** presented significant antibacterial effect to *Escherichia coli* (*E. coli*), through reported ROS-related damage pathway. Ultimately, the related inactivation rate of **Cu-FA** was determined as 99.76% at 200 μg mL^{-1}, while demonstrated negligible cytotoxicity against human cells.

QingPu Hospital Affiliated to Fudan University, Shanghai 201700, P. R. China. E-mail: liu.boya@qphospital.com

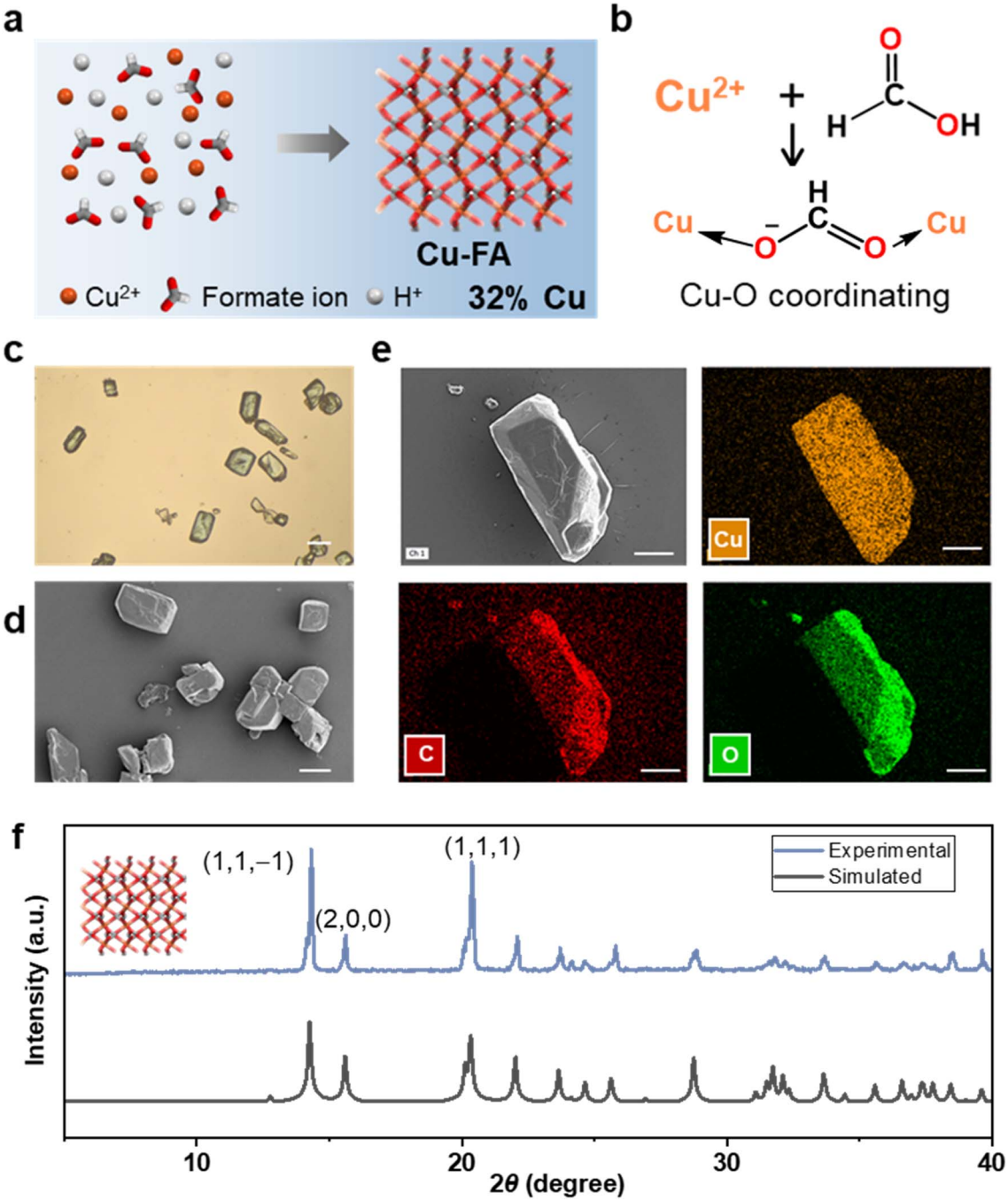

Fig. 1 Synthesis of **Cu-FA**. (a) Schematic illustration of the synthesis of **Cu-FA** by solvothermal reaction of Cu^{2+} and FA. (b) The two coordination sites in formate ion. (c) Optical image and (d) scanning electron microscope (SEM) image of **Cu-FA** crystals. The scale bars are 100 μm. (e) SEM image and energy dispersive spectroscopy (EDS) mappings of a **Cu-FA** crystal. The scale bars are 20 μm. (f) Experimental and simulated power X-ray diffractions of **Cu-FA**.

2. Materials and methods

2.1 Materials and general methods

All compounds were commercially available (Aladdin Chemical Reagents Co., Ltd) and used as received. HEK-293 and HUVEC cells were purchased from Fuheng Biotechnology Co., Ltd *E. coli* (ATCC25922) was provided by Hangzhou Yanqu Information Technology Co., Ltd. The optical photos were recorded by a XD-202 microscope, equipped with a Nikon D3500 camera. Fourier transform infrared (FT-IR) spectra were recorded using a Nicolet iS50 Spectrophotometer (Thermo-Scientific). The ROS levels were detected in a FACSAria III Flow Cytometry, using a ROS assay kit (Beyotime, Shanghai, China).

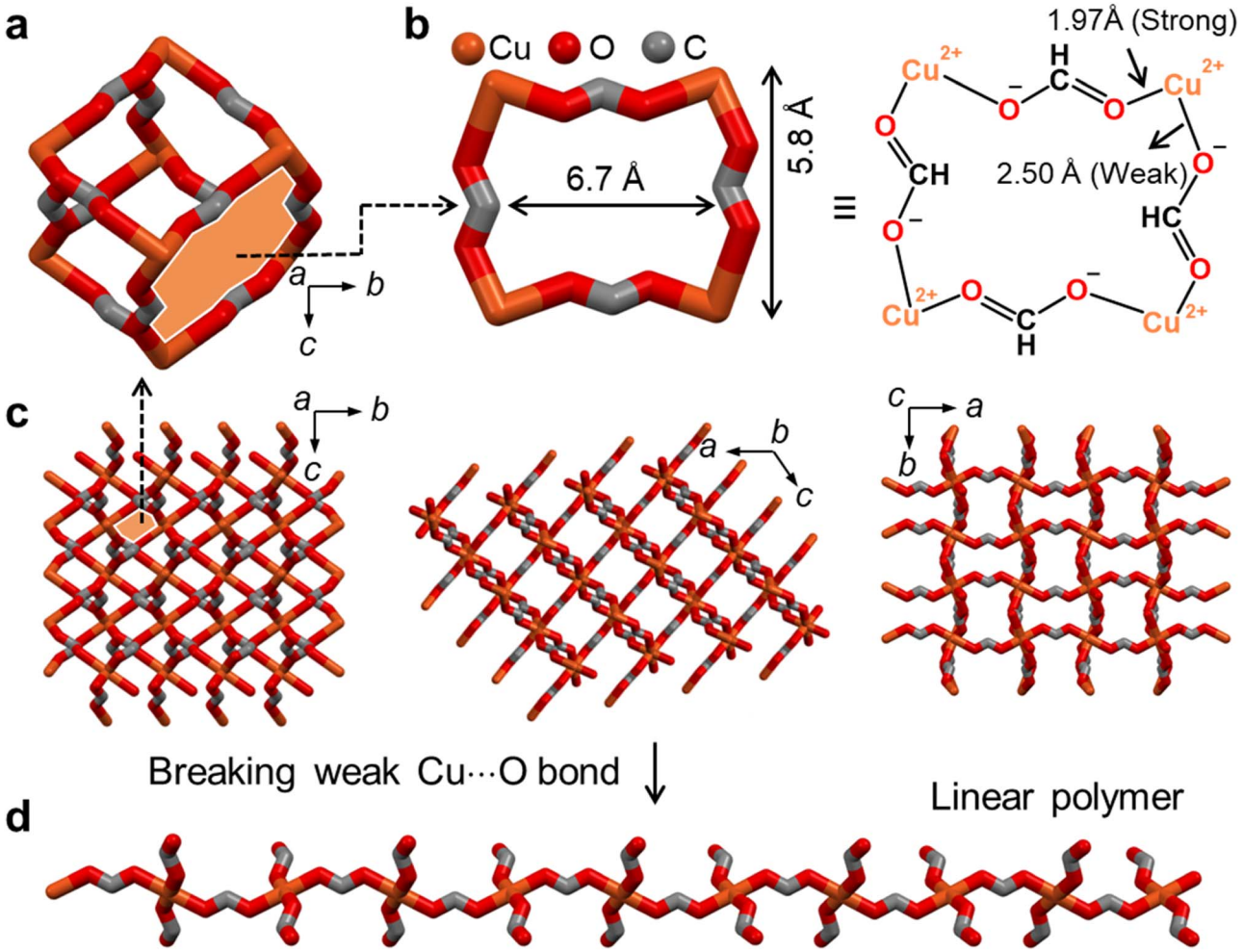

Fig. 2 Crystal structure of **Cu-FA**. (a) Crystal structure of the basic building block featuring a cubic configuration, viewed along *a* axis. (b) Crystal structure of one typical face of the cube, composed of four Cu^{2+} ions, four carbon atoms, and eight oxygen atoms. (c) Packing views of the crystal structure of **Cu-FA**. (d) Crystal structure of **Cu-FA** after cleaving the weak C–O···Cu bonds, characterized by a linear polymer. H atoms are simplified for clarity.

2.2 Synthesis of Cu-FA

$CuCl_2$ (4.00 mg, 0.03 mmol) and formic acid (4.14 mg, 0.09 mmol) were added to 1% dimethylamine aqueous solution (5 mL). The mixture was then heated at 90 °C for 10 h to generate light blue single crystals of **Cu-FA**, 5.2 mg (71% yield).

2.3 Density functional theory calculations

The electrostatic potential maps, the reduced density gradient (RDG) and corresponding non-covalent interaction (NCI) analyses were carried out with the Gaussian 16 software. Density functional theory (DFT) calculations were carried out using the M06-2X functional with the combination of the Grimme's D3 version of dispersion correction.[28] The basis set of 6-31G (d, p) was adopted for the energy calculations. The RDG was evaluated by Multiwfn package.[29]

2.4 Optical density measurements

E. coli (ATCC25922) suspension (10^6 CFU mL^{-1}) and **Cu-FA** at different concentrations were incubated statically in LB liquid medium at 37 °C for 10 hours. After incubation, the optical density (OD) of each group was measured at a wavelength of 600 nm using a microplate reader.

2.5 Scanning electron microscope measurement

The crystal samples were transferred onto silicon wafers and coated with gold nanoparticles. Scanning electron microscope (SEM) observations were carried out on a Verios G4 Field Emission scanning electron microscope combined with energy dispersive X-ray analysis.

2.6 Single crystal X-ray diffraction

Single crystal X-ray diffraction data were obtained on an Oxford Gemini A Ultra diffractometer (Mo-Kα, Atlas CCD detector). All non-hydrogen atoms were refined with anisotropic thermal

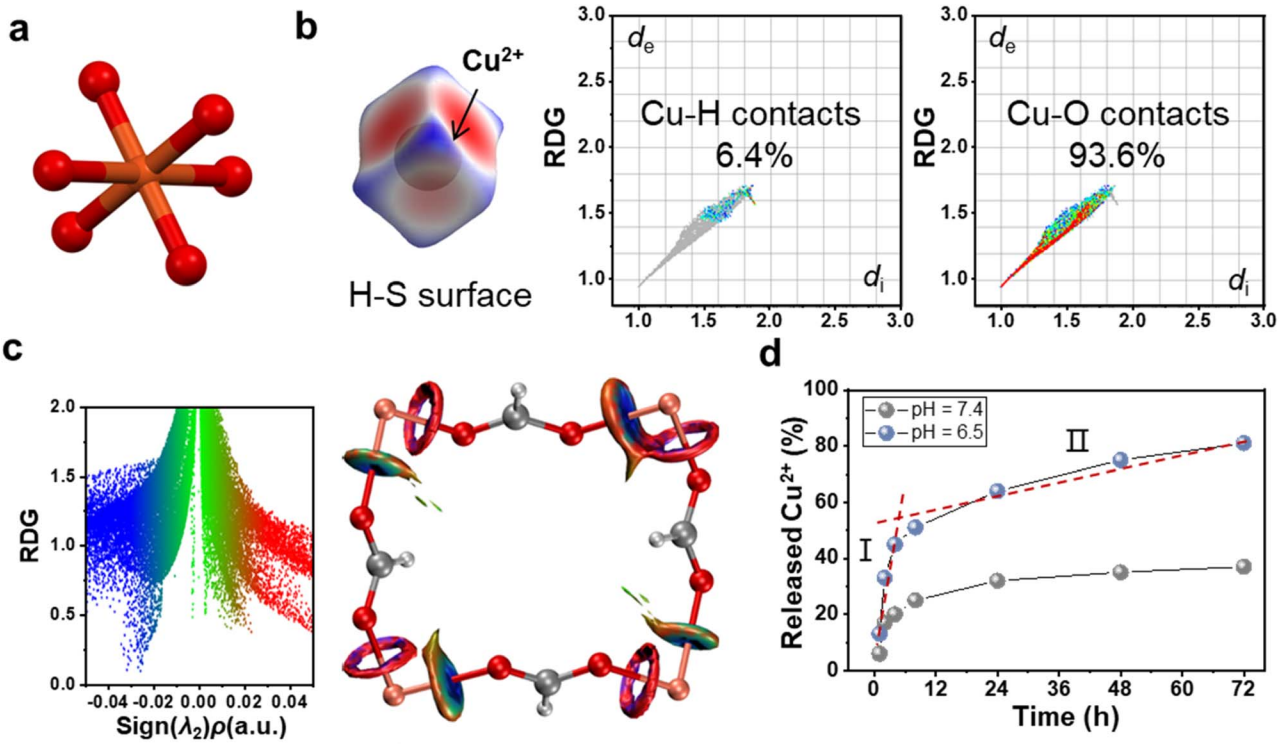

Fig. 3 DFT calculations. (a) The hexacoordinated configuration of one Cu^{2+} with eight O atoms. (b) H–S surface analyses of the central Cu^{2+}. (c) RDG and NCI analyses of **Cu-FA**. (d) Real-time Cu^{2+} release curve measured by ICP-OES at pH = 7.4 and 6.5. A cumulative release efficiency of 81% was achieved within 72 hours at PH 6.5, compared to 37% at Ph 7.4.

parameters and the hydrogen atoms were fixed at calculated positions and refined by a riding mode. The corresponding CIF files, which include structure factors, are available free of charge from the Cambridge Crystallographic Data Centre (CCDC) *via* www.ccdc.cam.ac.uk/data_request/cif. CCDC number, 2410570.

2.7 Power X-ray diffraction

Powder X-ray diffraction (PXRD) data were collected on a Rigaku Smartlab 9 kW advance X-ray diffractometer, operating at 40 kV/40 mA using the Cu-Kα line (λ = 0.15406 nm). PXRD Patterns were scanned over the 2θ range of 5–40° with a sweep speed of 10°/min.

2.8 Dilution plate smear method

Escherichia coli suspension (10^6 CFU mL^{-1}) and **Cu-FA** (200 μg mL^{-1}) were co-cultured in a 37 °C constant-temperature shaker for 10 hours. After incubation, the suspension was serially diluted 10-fold with sterile PBS solutions. Subsequently, 100 μL of the diluted suspension was evenly spread onto LB solid agar plates and incubated at 37 °C for 10 hours. Finally, the plates were photographed to count the colony-forming units.

2.9 Reactive oxygen species assay

Intracellular ROS levels were quantified using a commercial ROS assay kit following the manufacturer's protocol. Briefly, after treatment with different concentration of **Cu-FA**, *E. coli* was collected, washed twice with phosphate-buffered saline (PBS), and incubated with 10 μmol L^{-1} 2′,7′-dichlorodihydrofluorescein diacetate at 37 °C for 40 minutes in a dark room. Fluorescence intensity was subsequently measured by flow cytometry.

3. Results

3.1 Synthesis of Cu-FA

Originally, light blue crystals (Fig. 1c and d) characterized by a three-dimensional (3D) framework, were formed when heating a mixture of $CuCl_2$ and FA (n/n, 1/3) in dimethylamine aqueous solution at 90 °C for 12 hours. During solvothermal reaction, Cu···O coordination and crystallization occurred to produce the metal–organic framework, named **Cu-FA** (Fig. S1 and S2). Uniformly distributed Cu, C and O elements are observed throughout these crystals by energy dispersive spectroscopy (EDS) mappings (Fig. 1e and S3). To further obtain the precise topology structure of **Cu-FA**, SCXRD was subsequently employed. As shown in Table S1, **Cu-FA** crystallized in a monoclinic system (*C* 2/*C* space group), with cell lengths of 13.7, 8.7 and 8.8 Å for *a*, *b*, and *c* axes, respectively, and cell angles of 90°, 123.8°, and 90° for or α, β, and γ, respectively. The discrepancy factor *R* was determined as 1.95%, allowing precise structural parameters, for example, atomic positions, bond lengths, bond angles, *etc.* Furthermore, the experimental power X-ray diffraction (PXRD) pattern well matched with the simulation based on the SCXRD data, thus confirming the high purity of the

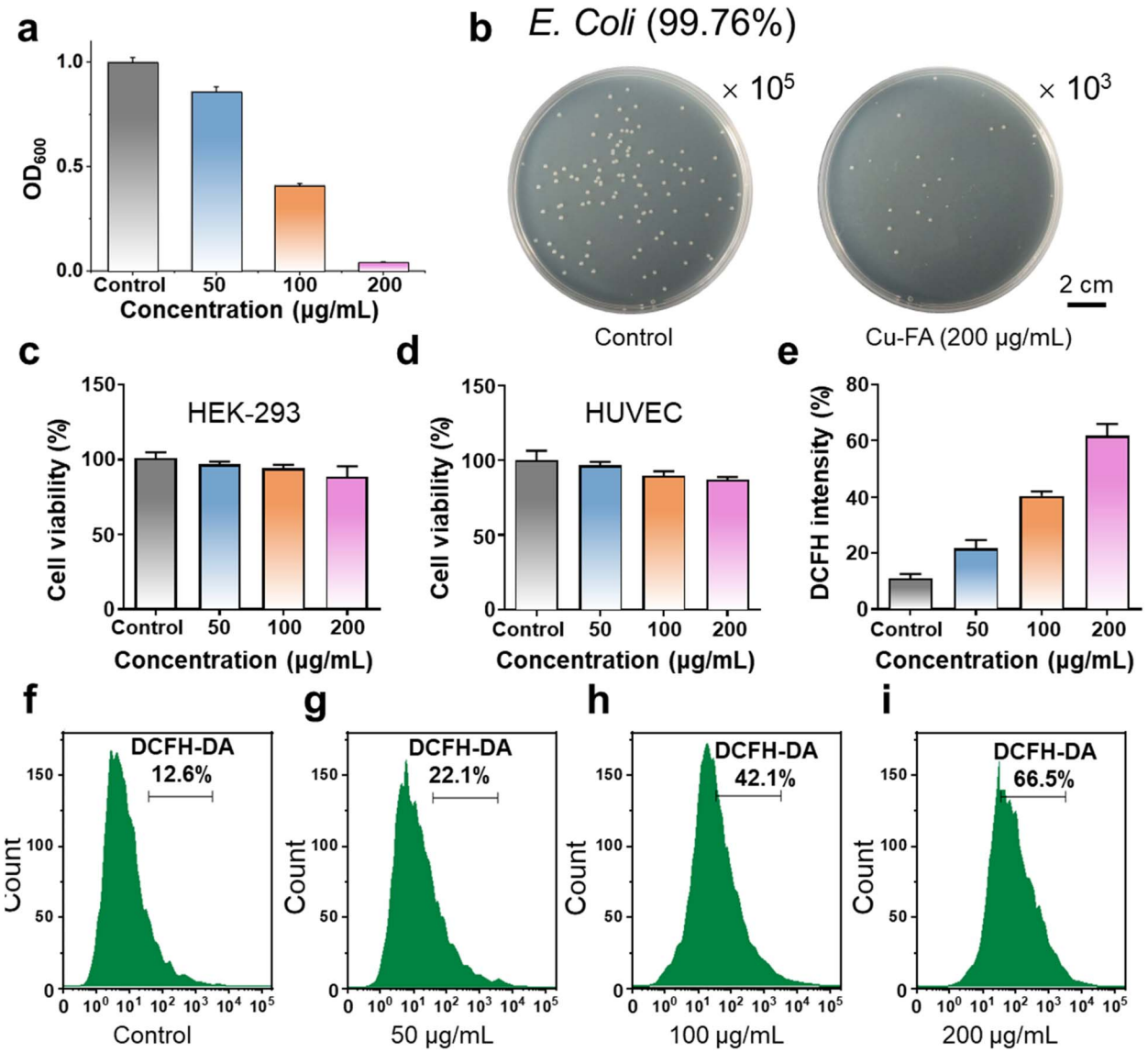

Fig. 4 *In vitro* antibacterial performance of **Cu-FA**. (a) OD measurements of different concentrations of **Cu-FA**. (b) Representative images of bacterial colonies formed by *E. coli* without (left, 10^5 diluted) and with 200 μg mL^{-1} **Cu-FA** (right, 10^3 diluted). The scale bar is 2 cm. Cell viability measurements of (c) HEK-293 and (d) HUVEC cells with different concentrations of **Cu-FA**. (e) ROS assay with (f) 0, (g) 50 (h) 100 and (i) 200 μg mL^{-1} **Cu-FA**.

synthesized powder material. Specifically, $2\theta = 14.2, 15.6, 20.4°$ represent crystal surfaces of (1,1,−1), (2,0,0) and (1,1,1), respectively. Benefiting from its ordered 3D architecture, **Cu-FA** exhibited excellent thermal and water stability (Fig. S4 and S5), which lays a solid foundation for subsequent antibacterial applications.

3.2 Crystal structure of Cu-FA

In preparation for subsequent antibacterial applications, we conducted a detailed analysis of the packing structure of **Cu-FA** using SCXRD results. The architecture of **Cu-FA** features a cubic building block, composed of eight Cu^{2+} and twelve formate ions ($HCOO^-$) as its vertices and edges, respectively (Fig. 2a and S6). And each face of the cube (Fig. 2b) consists of four Cu^{2+}, four carbon atoms, and eight oxygen atoms. Moreover, two types of Cu···O coordination bonds were observed with bond lengths of 1.97 and 2.50 Å for C=O and C–O groups, respectively. This implied that the difference in bond energy for the two Cu···O coordination bonds, suggesting that **Cu-FA** undergoes sequential cleavage of Cu···O coordination bonds under the acidic microenvironment. Specifically, the weak C–O···Cu coordination bonds (corresponding to 2.50 Å) preferentially cleaved, triggering the transformation of **Cu-FA** from a 3D framework into linear polymers (Fig. 2c and d). Subsequently, C=O···Cu coordination bonds break, leading to further degradation of the continuous polymer into free Cu^{2+} ions and formate anions. The multilevel degradation pathways of **Cu-FA** avoid the rapid surge of Cu^{2+} concentration, thereby ensuring biocompatibility.

In order to get a deep insight into the release kinetics of Cu^{2+}, density functional theory (DFT) calculations were carried out (Fig. S7). Copper ions in **Cu-FA** adopt hexacoordinated configuration with O atoms, exhibiting an octahedral geometry (Fig. 3a and S8). For the central Cu^{2+}, we conducted Hirshfeld (H–S) surface analyses,[30–32] as shown in Fig. 3b. Cu–O interactions dominate the surface contacts, accounting for 93.6%, underscoring the critical role of Cu–O bond energy in stabilizing **Cu-FA**. Subsequently, we conducted reduced density gradient (RDG) and non-covalent interaction (NCI) analyses to examine the Cu–O interactions.[33–36] The analyses (Fig. 3c) revealed distinct features: one presented a circular ring, corresponding to weak coordinating (2.5 Å); another presented a circular plane, corresponding to strong coordinating (1.97 Å). Finally, ICP-OES was used to real-time detection of Cu^{2+} concentrations. Under acidic conditions, **Cu-FA** was degraded resulted by the protonation of organic ligand and the ions exchange between H^+ and Cu^{2+}.[37,38] As shown in Fig. 3d, the results indicated that at pH 6.5, a cumulative release efficiency of 81% was achieved within 72 hours, which followed a biphasic profile consisting of an initial rapid release stage followed by a sustained slower phase. After the Cu release, **Cu-FA** was found decomposed into smaller irregular particles, with a diameter of 1 μm (Fig. S9). As a comparison, only 37% Cu^{2+} was released at Ph 7.4, verifying the acid-accelerated multistage Cu^{2+} release mechanism.

3.3 *In vitro* antibacterial performance of Cu-FA

Bacterial infections critically impair wound healing processes, leading to detrimental consequences for human health. Among pathogenic bacteria, Gram-negative strains are particularly problematic due to their protective outer membranes and harmful endotoxins.[39–44] Infected bacterial wounds were reported to exhibit an acidic microenvironment[45] as a result of metabolite accumulation (acetic acid, lactic acid, and malic acid), inflammatory responses, and localized hypoxia, providing a change for the antibacterial applications of **Cu-FA**. Specifically, under the bacterial infected acidic microenvironment, **Cu-FA** will undergo progressive degradation to release Cu^{2+}, which have been proven to produce ROS and induce bacterial death. Here, *E. coli* was used as a representative Gram-negative strain for antibacterial research. Firstly, the antibacterial performance of **Cu-FA** was evaluated by measuring the optical density (OD) at 600 nm. The result (Fig. 4a) shows significant antibacterial performance when the concentration of **Cu-FA** exceeding 200 μg mL^{-1}. Subsequently, the survival rate was measured by dilution plate smear method. After co-incubation for 10 hours, the photographs of **Cu-FA** (10^3 diluted) and control (10^5 diluted) were shown in Fig. 4b. Accordingly, the *E. coli* concentrations were determined as 2.00×10^4 CFU mL^{-1} for **Cu-FA** (200 μg mL^{-1}) and 8.50×10^6 CFU mL^{-1} for the control (Fig. 4b). Accordingly, the inactivation rate of *E. coli* was calculated as 99.76% for 200 μg mL^{-1} **Cu-FA**, demonstrating a clear advantage over other Cu-MOF reported in the literature (Table S2). Furthermore, HEK-293 and HUVEC cells were used to evaluate the biocompatibility of **Cu-FA** using MTT method. At high concentration of 200 μg mL^{-1}, cell viability remained unaffected, demonstrating the excellent biocompatibility of **Cu-FA** (Fig. 4c and d). Ultimately, to validate the previously reported ROS-induced antimicrobial mechanism, a dichloro-dihydrofluorescein (DCFH-DA) probe was employed to detect the ROS content. As expected, flow cytometry revealed the increase in ROS level with escalating **Cu-FA** concentrations (Fig. 4e–i), confirming the reported oxidative damage mechanism induced by Cu^{2+} ion.[10,11] Furthermore, for broader applications, **Cu-FA** can also be fabricated in film form *via* calendaring with 10% polytetrafluoroethylene (Fig. S10).[46] Overall, the high-Cu-content **Cu-FA** exhibited potential antibacterial activities through *in vitro* experiments.

4. Conclusions

This study achieved a high-copper-content MOF through direct solvothermal reaction of $CuCl_2$ and formic acid. SCXRD analyses revealed an exceptional copper loading capacity of 32% in the 3D framework, which exhibited a unique multistage copper release protocol. As a result, the MOF material exhibited an effective *in vitro* antibacterial action against *E. coli* with an inactivation rate of 99.76%, while exhibiting remarkable biocompatibility, confirmed by HEK-293 and HUVEC cells. Overall, this study proposed a new approach for the synthesis of high-copper-content MOF materials with multistage Cu release kinetics, and also providing new insights for the development of next-generation antibacterial Cu MOFs.

Author contributions

Boya Liu: conceptualization, investigation, writing–original draft, writing–review and editing. Xueqi Zheng: conceptualization, writing–review and editing.

Conflicts of interest

There are no conflicts to declare.

Data availability

CCDC 2410570 contains the supplementary crystallographic data for this paper.[47]

The datasets generated during and/or analysed during the current study are available from the corresponding author on reasonable request.

Supplementary information (SI): crystallographic data and SEM images. See DOI: https://doi.org/10.1039/d5ra08205f.

Notes and references

1 J. Mei, D. Xu, L. Wang, L. Kong, Q. Liu, Q. Li, X. Zhang, Z. Su, X. Hu, W. Zhu, M. Ye, J. Wang and C. Zhu, *Adv. Mater.*, 2023, **35**, 2303432.
2 Q. Huang, J. Liang, Q. Chen, X. Jin, M. Niu, C. Dong and X. Zhang, *Nano Today*, 2023, **51**, 101911.

3 X. Zhang, Z. Wang, Q. Liu, X. Hu, J. Mei, D. Xu, J. Zhou, X. Zhang, Q. Li, H. Chen, Z. Su, W. Zhu and C. Zhu, *Nano Today*, 2024, **54**, 102092.
4 Y. Ma, J. Huang, S. Song, H. Chen and Z. Zhang, *Small*, 2016, **12**, 4936.
5 B. Li, X. Wang, L. Chen, Y. Zhou, W. Dang, J. Chang and C. Wu, *Theranostics*, 2018, **8**, 4086.
6 H. Liu, X. Wei, H. Peng, Y. Yang, Z. Hu, Y. Rao, Z. Wang, J. Dou, X. Huang, Q. Hu, L. Tan, Y. Wang, J. Chen, L. Liu, Y. Yang, J. Wu, X. Hu, S. Lu, W. Shang and X. Rao, *Adv. Mater.*, 2024, **36**, 2412154.
7 X. Wang, M. Shan, S. Zhang, X. Chen, W. Liu, J. Chen and X. Liu, *Adv. Sci.*, 2022, **9**, 2104843.
8 Y. Yang, J. Wang, S. Huang, M. Li, J. Chen, D. Pei, Z. Tang and B. Guo, *Natl. Sci. Rev.*, 2024, **11**, nwae044.
9 Y. Wang, X. Zhao, X. Zhou, J. Dai, X. Hu, Y. Piao, G. Zu, J. Xiao, K. Shi, Y. Liu, Y. Li and L. Shi, *J. Control. Release*, 2024, **368**, 740.
10 Y. Liu, Z. Guo, F. Li, Y. Xiao, Y. Zhang, T. Bu, P. Jia, T. Zhe and L. Wang, *ACS Appl. Mater. Interfaces*, 2019, **11**, 31649.
11 S. Yao, Y. Wang, J. Chi, Y. Yu, Y. Zhao, Y. Luo and Y. Wang, *Adv. Sci.*, 2022, **9**, 2103449.
12 M. Wang, R. Li, S. Sheng, H. Yang, X. Tang, J. Wang, F. Wang, Q. Zhang, L. Bai, X. Chen, J. Gao, X. Ren, H. Liu and J. Su, *Nano Today*, 2025, **63**, 102753.
13 D. Yang, J. Yi, X. Li, S. Zhang, Y. Xiang, X. Liu, Z. Shan and H. Wang, *Food Sci. Hum. Well.*, 2025, **14**, 9250060.
14 Y. Zhong, X. Zheng, Q. Li, X. Loh, X. Su and S. Zhao, *Biosens. Bioelectron.*, 2023, **224**, 115033.
15 F. Mo, S. Zhong, T. You, J. Lu and D. Sun, *ACS Appl. Mater. Interfaces*, 2023, **15**, 52114.
16 S. Chen, J. Chen, X. Wang, Z. Yang, J. Lan, L. Wang, B. Ji and Y. Yuan, *Carbohydr. Polym.*, 2025, **348**, 122894.
17 Y. Li, X. Zhang, W. Hou, Z. Zhou, S. Zhang, H. Guo, J. Zhang, J. Xu and L. Wang, *Appl. Catal. B-Environ. Energy*, 2026, **380**, 125758.
18 M. N. Ahamad, M. S. Khan, M. Shahid and M. Ahmad, *Dalton Trans.*, 2020, **49**, 14690.
19 S. Kim, H. Lee, J.-M. Suh, M. H. Lim and M. Kim, *Inorg. Chem.*, 2020, **59**, 17573.
20 A. Paul, A. P. C. Ribeiro, A. Karmakar, M. F. C. G. D. Silva and A. J. L. Pombeiro, *Dalton Trans.*, 2016, **45**, 12779.
21 Y. Zhao, Y. Chai, L. Ding, S. Wang, Y. Wang, L. Ma and B. Zhao, *Arab. J. Chem.*, 2023, **16**, 104878.
22 M. Kim, Y. Lee and H. R. Moon, *Acc. Chem. Res.*, 2024, **57**, 2347.
23 J. G. Flores, R. Delgado-Garcia and M. Sanchez-Sanchez, *Catal. Today*, 2022, **390**, 237.
24 U. N. Hazarika, K. Sonowal, A. T. T. Mostako and P. Khakhlary, *Inorg. Chem.*, 2025, **64**, 15748.
25 U. N. Hazarika, J. Borah, A. Kakoti, R. Brahma, K. Sarmahc, A. K. Guha and P. Khakhlary, *Mater. Adv.*, 2023, **4**, 6304.
26 X. Wang, L. Gan, S. Zhang and S. Gao, *Inorg. Chem.*, 2004, **43**(15), 4615.
27 X. Wang, H. Wei, Z. Wang, Z. Chen and S. Gao, *Inorg. Chem.*, 2005, **44**, 572.
28 S. Grimme, J. Antony, S. Ehrlich and H. Krieg, *J. Chem. Phys.*, 2010, **132**, 154104.
29 T. Lu and F. J. Chen, *Comput. Chem.*, 2012, **33**, 580.
30 P. R. Spackman, M. J. Turner, J. J. Mckinnon, S. K. Wolff, D. J. Grimwood, D. Jayatilaka and M. A. Spackman, *J. Appl. Crystallogr.*, 2021, **54**, 1006.
31 A. Tarahhomi, M. Pourayoubi, J. A. Golen, P. Zargaran, B. Elahi, M. A. L. Ramírez and T. M. Percino, *Acta Cryst.*, 2013, **69**, 260.
32 M. Guin, S. Khanna, S. B. Elavarasi and P. Sarkar, *Chem. Sci.*, 2020, **132**, 81.
33 G. Saleh, C. Gatti and L. L. Presti, *Comput. Theory Chem.*, 2012, **998**, 148.
34 G. Saleh, C. Gatti and L. L. Presti, *Comput. Theory Chem.*, 2015, **1053**, 53.
35 G. Saleh, C. Gatti, L. L. Presti and J. Contreras-García, *Chem. Eur. J.*, 2012, **18**, 15523.
36 L. Leherte, *Theor. Chem. Acc.*, 2021, **140**, 9.
37 F. Duan, X. Feng, X. Yang, W. Sun, Y. Jin, H. Liu, K. Ge, Z. Li and J. Zhang, *Biomaterials*, 2017, **122**, 23.
38 P. Mhettar, N. Kale, J. Pantwalawalkar, S. Nangare and N. Jadhav, *Admet Dmpk*, 2024, **12**, 27.
39 U. Theuretzbacher, B. Blasco, M. Duffey and L. J. Piddock, *Nat. Rev. Drug Discovery*, 2023, **22**, 957.
40 M. K. Gugger and P. J. Hergenrother, *Nature*, 2024, **625**, 451.
41 E. R. Rojas, G. Billings, P. D. Odermatt, G. K. Auer, L. Zhu, A. Miguel, F. Chang, D. B. Weibel, J. A. Theriot and K. C. Huang, *Nature*, 2018, **559**, 617.
42 C. K. Dzuvor, H.-H. Shen, V. S. Haritos and L. He, *ACS Nano*, 2024, **18**, 4478.
43 A. L. Santos, D. Liu, A. van Venrooy, J. L. Beckham, A. Oliver, G. P. Tegos and J. M. Tour, *ACS Nano*, 2024, **18**, 3023.
44 B. Benyahia, N. Taib, C. Beloin and S. Gribaldo, *Nat. Rev. Microbiol.*, 2024, **23**, 41.
45 W. Wang, Y. Cui, X. Wei, Y. Zang, X. Chen, L. Cheng and X. Wang, *ACS Nano*, 2024, **18**, 15845.
46 H. Wang, S. Zhao, Y. Liu, R. Yao, X. Wang, Y. Cao, D. Ma, M. Zou, A. Cao, X. Feng and B. Wang, *Nat. Commun.*, 2019, **10**, 4204.
47 CCDC 2410570: Experimental Crystal Structure Determination, 2026, DOI: 10.5517/ccdc.csd.cc2lxdb8.